PNAS RESEARCH ARTICLE | ENGINEERING OPEN ACCESS

Self-adaptive dislocation morphing ductilizes a refractory high-entropy alloy across an ultrawide temperature spectrum

Xichen Zhou[a,b,1], Qianyong Zhu[a,b,1], Hongliang Dong[c,d,1], Xiao Liang[a,b], Qihan Jia[a,b], Cheng Zhang[a,b,2], Jian He[a,b], Wenting He[a,b], Yuye Wu[a,b], Yi Ru[a,b], Bin Chen[c,d], Robert O. Ritchie[e,2], Hongbo Guo[a,b,2], and Shiteng Zhao[a,b,2]

Affiliations are included on p. 8.

Contributed by Robert O. Ritchie; received October 13, 2025; accepted November 25, 2025; reviewed by Rui Feng, Peter K. Liaw, and Qingsong Pan

Metals usually fracture catastrophically at cryogenic temperatures and soften rapidly at high temperatures. This dilemma arises from the incompatibility of strengthening mechanisms across vast temperature regimes. Here, this work unveils a self-adaptive dislocation morphing mechanism in a model NbTaTi-based refractory high-entropy alloy (RHEA) that enables exceptional strength and ductility from 4 K to 1673 K. At cryogenic temperatures, dislocation kinking coupled with deformation twinning suppresses the ductile-to-brittle transition. At ambient conditions, the sequential activation of edge and screw dislocations sustains work hardening. At elevated temperatures, enhanced dislocation interactions generate jogs, multijunctions, and helical dislocations, promoting superplasticity up to 250%. This intrinsic, temperature-responsive evolution of dislocation modes offers a defect engineering strategy for designing RHEAs capable of enduring extreme environments.

refractory high-entropy alloys | ultrawide temperature range | tensile properties | dislocation mechanism

Significance

Refractory alloys hold immense promise for high-temperature applications but are often limited by poor ductility. This work demonstrates in a model $Nb_{40}Ta_{25}Ti_{15}Hf_{15}Zr_5$ refractory high-entropy alloy (RHEA) that self-adaptive dislocation mechanisms can operate in response to varying temperatures. As such, the alloy remains ductile even at cryogenic temperatures and turns superplastic at high temperatures. The versatile morphing of dislocations over an ultrawide temperature window in a singular alloy establishes a defect engineering design principle for high-performance materials facing extreme conditions.

The pursuit of advanced technologies, from deep-space exploration and superconducting systems to next-generation fusion reactors, demands structural materials that retain exceptional mechanical integrity across ultrawide temperature extremes. Acquiring high strength while maintaining ductility over such a vast temperature span presents an insurmountable challenge for off-the-shelf structural alloys. Many nickel-based superalloys, the current high-temperature benchmark, suffer catastrophic embrittlement below 77 K and approach fundamental limits above ~1,400 K, restricting their development potential (1). Refractory high-entropy alloys (RHEAs), engineered from high-melting-point elements, have emerged as promising alternatives due to their superior strength at elevated temperatures (2, 3). However, their widespread adoption remains hindered by poor ambient-temperature ductility and severe low-temperature embrittlement.

Recent efforts to overcome these limitations have focused on nonequiatomic NbTaTi-based systems. Prior work demonstrated that the $Nb_{40}Ta_{25}Ti_{15}Hf_{15}Zr_5$ (atomic percent, at.%) alloy achieves remarkable room-temperature formability alongside superior tensile strength-ductility combinations from 77 to 1,373 K (4). Building on this, Cook *et al.* revealed that controlled activation of kink bands enables an unprecedented synergy of strength and fracture toughness across 77 to 1,473 K in these systems (5). Complementary studies further highlight their promising high-temperature creep properties (6, 7) and oxidation resistance (8), establishing NbTaTi-based alloys as a pivotal material system targeting extreme applications (9–11).

Due to the absence of close-packed planes in the BCC structure, the dislocation activity in refractory alloys exhibits anomalous slip, with all {110}, {112}, and {123} planes potentially being activated (12–14). This leads to complex dislocation configurations, such as metastable dislocation junctions (15), multijunctions (16), or networks. In RHEAs, Wang *et al.* observed that the rugged atomic energy landscape provides additional slip pathways for dislocations, which is advantageous for plasticity (17). However, the influence of dislocations on the mechanical properties of RHEA remains contradictory: Trusu *et al.* studied the drastically different deformation mechanisms between NbTaTiHfZr and NbTaMoWV alloys, concluding that the activation and motion of more screw dislocations are key to plastic deformation, resulting from their different dislocation core (18). Conversely, other researchers proposed that edge dislocations control yield strength and dominate deformation on NbTaTiV (19) and CrMoNbV (20, 21) alloys. Recent research on refractory alloys has further explored alloy design (22, 23), dislocation tailoring to enhance properties (24), and cryogenic twinning-induced plasticity (TWIP) (25). However, these efforts primarily focus on narrow temperature windows. A unified,

Author contributions: X.Z., Q.Z., H.D., X.L., Q.J., and C.Z. performed research; J.H., W.H., Y.W., Y.R., B.C., R.O.R., H.G., and S.Z. analyzed data; and C.Z., R.O.R., H.G., and S.Z. wrote the paper.

Reviewers: R.F., Shanghai Jiaotong University; P.K.L., The University of Tennessee Knoxville; and Q.P., Institute of Metal Research, the Chinese Academy of Sciences.

The authors declare no competing interest.

[1]X.Z., Q.Z., and H.D. contributed equally to this work.

[2]To whom correspondence may be addressed. Email: bht0095@tmslab.cn, ritchie@berkeley.edu, guo.hongbo@buaa.edu.cn, or szhao@buaa.edu.cn.

This article contains supporting information online at https://www.pnas.org/lookup/suppl/doi:10.1073/pnas.2529140123/-/DCSupplemental.

Published January 2, 2026.

experimentally grounded framework that describes how dislocation type, morphology, and interactions evolve continuously with temperature, and whether such evolution can sustain ductility and strength across an ultrawide temperature span, is still lacking.

The current work bridges this gap through a nonequiatomic $Nb_{40}Ta_{25}Ti_{15}Hf_{15}Zr_5$ (at.%) RHEA (subsequently termed as Nb40 alloy) by investigating its tensile behavior across an ultrawide 1,670 K range (4 to 1,673 K). It is revealed that a sequential, temperature-driven evolution of self-adaptive dislocation mechanisms is established that sustains strength-ductility synergy. This systematic dissection of continuously adaptive dislocation physics within a single RHEA over 1,670 K resolves the long-standing ductility challenge across extremes, and establishes a mechanistic understanding for designing dislocation-mediated, temperature-resilient alloys.

Results

Temperature Dependence of Tensile Properties. The tensile behavior of Nb40 was systematically evaluated over a wide temperature range from 4 to 1,673 K (Fig. 1). All specimens exhibited an initial equiaxed microstructure with an average grain size of 19.6 ± 7.1 μm (Fig. 1*A*). As shown in Fig. 1*B*, the alloy demonstrates a yield strength of nearly 800 MPa at room temperature (298 K), with a fracture elongation of approximately 25%. Notably, even at cryogenic temperature (4 K), Nb40 retains 10% tensile ductility with pronounced necking (*SI Appendix*, Fig. S3), indicating the absence of a detectable ductile-to-brittle transition—a rare feature among refractory alloys, where low-temperature embrittlement is often pronounced.

With increasing temperature, the yield strength decreases monotonically, consistent with thermally activated dislocation motion. At 1,073 K, a modest drop in elongation is observed, associated with the onset of grain-boundary-related cleavage features. Above 1,273 K, the deformation mechanism shifts dramatically; Nb40 enters a special regime of superplasticity, with elongation rising steeply and reaching ~250% at 1,673 K (Fig. 1*B*). X-ray diffraction (XRD) unequivocally confirms the alloy's preservation of a single-phase body-centered cubic (BCC) structure, with no phase transformations across the broad 4 to 1,673 K temperature range (Fig. 1*C*). Complementarily, atomic-scale energy-dispersive X-ray spectroscopy (EDS) detects no compositional fluctuations even after extended aging (*SI Appendix*, Fig. S4). This compelling evidence establishes that the alloy's remarkable superplasticity stems neither from phase transitions nor chemical segregation. Remarkably, this high-temperature superplasticity is realized with comparatively coarse grain sizes and at substantially higher strain rates than the demanding requirements for conventional structural alloys and ceramics (33) (ultrafine grains ≤ 5 μm and strain rates ≤ 10^{-4} s^{-1}) (34), nanoscale samples (35) or alloys reliant on elaborate processing routes (36).

The combined properties of Nb40 (Fig. 1*D*), including high strength with moderate work hardening, tunable superplastic formability, absence of ductile-to-brittle transition, and exceptional phase stability across an extremely broad temperature window, highlight

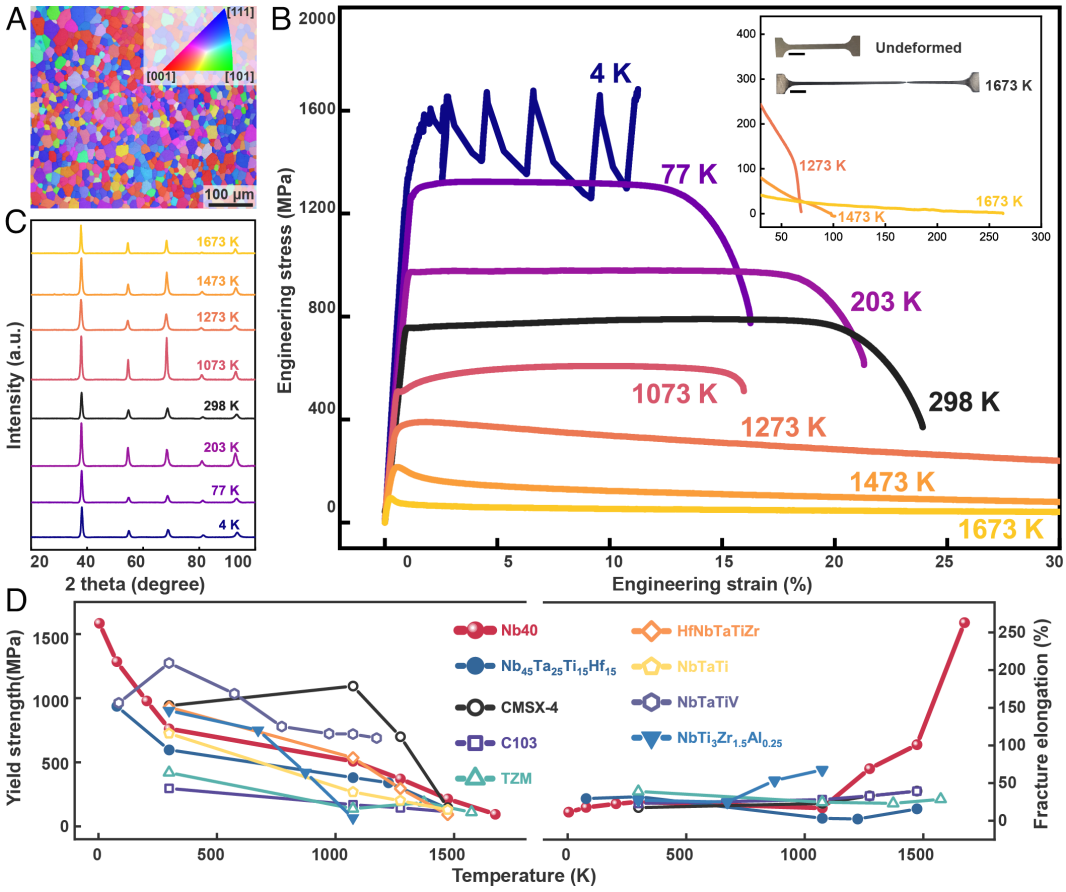

Fig. 1. Tensile properties of Nb40 alloy across an ultrawide temperature range. (*A*) The EBSD orientation map of the original equiaxed grain structure and average grain size is 19.6 ± 7.1 μm. (*B*) Tensile stress *vs.* strain curves of the alloy from 4 to 1,673 K, with the inset showing complete deformation curves for 1,273 to 1,673 K (scale bar in the inset: 10 mm). (*C*) X-ray diffraction results confirm that the alloy retains a single-phase BCC structure across the range of temperatures tested. (*D*) Comparison of yield strength and elongation between Nb40 and several high-temperature structure materials, including $Nb_{45}Ta_{25}Ti_{15}Hf_{15}$ (5), single-crystal CMSX-4 (Ni-based) (26), C103 (Nb-based) (27), TZM (Mo-based) (28), NbTaTi (compressive) (29), NbTaTiV (compressive) (30), $NbTi_3Zr_{1.5}Al_{0.25}$ (31), and HfNbTaTiZr (compressive) (32) (refractory high-entropy alloys).

the advantages of this alloy over other commercial refractory alloys and RHEAs (5, 26–32).

Temperature Dependence of the Deformation Mechanisms. To elucidate the sequential activation of deformation mechanisms in the Nb40 alloy at room temperature, high-energy X-ray diffraction (HEXRD) measurements were performed using synchrotron radiation at the Shanghai Synchrotron Radiation Facility (SSRF) (Fig. 2). Anisotropic peak broadening in the in situ patterns was quantified using a modified Williamson–Hall analysis (37) that incorporates the dislocation contrast factor C to distinguish edge- and screw-type characters of dislocations (38). Further details of this analysis are given in the Methods and Materials section. Linear fits of the modified broadening measure ΔK^2 versus K^2C (ΔK and K are broadening-related parameters) were performed for model pure dislocation characters; the relative quality of these fits (reported as R^2 in Fig. 2*D*) indicates the dominant dislocation character at each stage of deformation.

In situ X-ray diffraction (XRD) analysis at room temperature shows strong, anisotropic peak broadening during early plasticity. The modified Williamson–Hall analysis yields substantially better agreement with an edge dislocation model than with a screw dislocation model (Fig. 2 *B–D*), indicating that fast, edge-like segments dominate early plastic flow and help relax local stress concentrations (20, 39). The evolution of fit quality with strain follows a three-stage trend that reflects the macroscopic work-hardening curve: (I) intense dislocation multiplication with high fit quality, (II) slowing of simple dislocation motion accompanied by the emergence of complex, nonideal configurations (reduced fit quality), and (III) saturation of activity with stabilized fits.

Postmortem transmission electron microscopy (TEM) provides direct validation and deeper mechanistic insight, corroborating the in situ XRD findings on dislocation activities in the deformed Nb40 alloy. To investigate the evolution of dislocation structures across key deformation stages, we present specimens deformed to representative plastic strains. During the early stage (ε = 1%, Fig. 2*E*), the dislocation density increases rapidly with edge dislocations dominating the plasticity. As strain increases, strain-hardening approaches equilibrium and dislocation configurations evolve from initial dual slip to multislip systems (ε = 5%, Fig. 2*F*), albeit maintaining a planar slip morphology. The sequential activation of edge-screw dislocations has not been observed in previous postfailure analysis work (5). Note that the slip plane transitions from dominant {110} to increasing {112} activity (*SI Appendix*, Figs. S6 and S7). This reconfiguration of dislocations manifests as pronounced XRD peak broadening and underpins the enhanced tensile strength. As strain accumulates, planar slip becomes insufficient for homogeneous deformation. Nonplanar slip mechanisms, particularly near grain boundaries, emerge to accommodate further strain (ε = 15%, Fig. 2*G*). The activation of complex dislocation typically necessitates a higher critical resolved shear stress (CRSS) (39). This shift sustains dislocation multiplication, enabling a characteristic strength-ductility balance. At the later stage of plasticity, nonplanar slip fully develops (as-fractured, Fig. 2*H*), corresponding to the flattened fitting quality (Stage III, Fig. 2*D*).

Taken together, room-temperature deformation reflects a competition between I) sequential activation of edge-to-screw segments, II) a planar to nonplanar slip transition, and III) the emergence of complex dislocation structures. This competition produces moderate, sustained work hardening and reconciles high strength with appreciable ductility.

Lowering temperature strongly alters the morphology and balance of the dislocation character (Fig. 3). As temperature falls toward 203 K, nonscrew segments become more mobile and can escape to free surfaces, leaving a higher fraction of ½[111] screw segments (Fig. 3 *E* and *F* and *SI Appendix*, Fig. S8). Impediment of these screw segments promotes the formation of localized kink structures, serving as an adaptive response that relieves stress

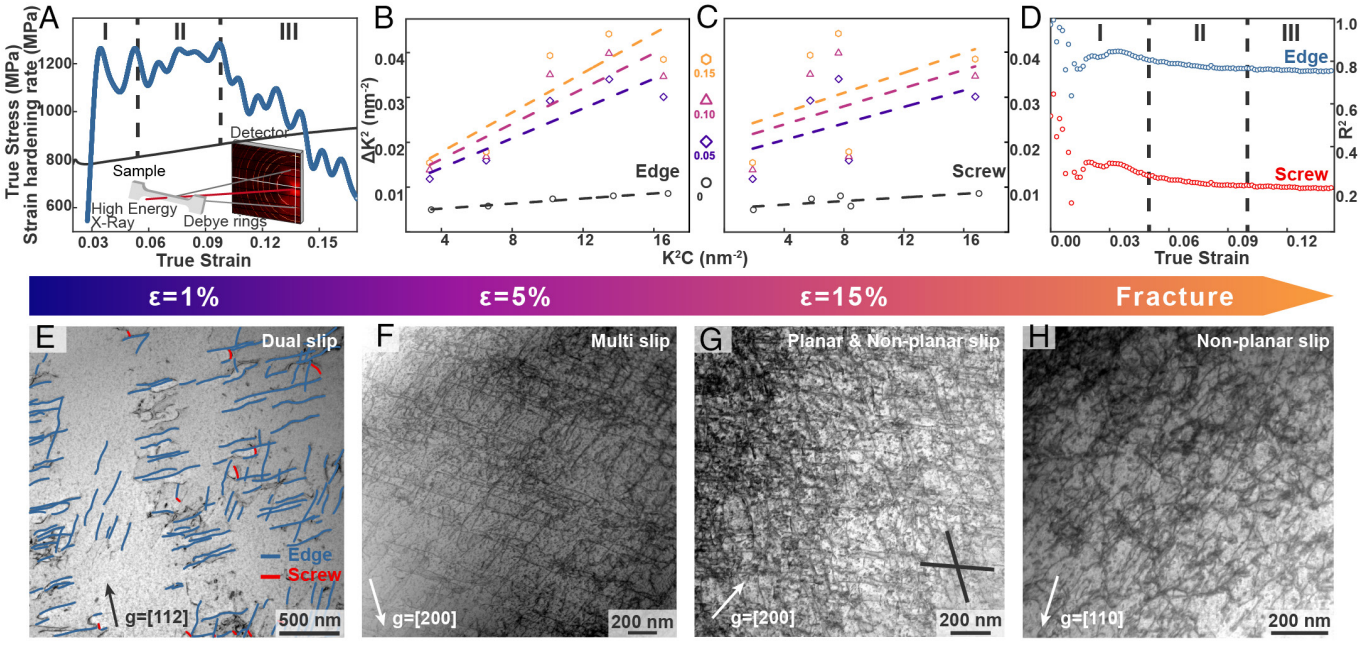

Fig. 2. The sequential activation of multiple dislocation mechanisms for Nb40 alloy at room temperature (298 K). (*A*) The work hardening plot reveals three deformation stages: I. strengthening regime (1% strain), II. balanced regime (5% strain), and III. softening regime (15% strain). (*B–D*) The analysis of diffraction peak broadening based on the modified Williamson-Hall method for the in situ synchrotron high-energy X-ray diffraction. The fitting linear of ΔK^2 versus K^2C for the (*B*) pure edge dislocation, (*C*) pure screw dislocation, and (*D*) their corresponding statistical R^2 at different strains, the fitting results similarly exhibit three-stage features. Dislocation morphology at (*E*) 1% strain, (*F*) 5% strain, (*G*) 15% strain, and (*H*) fracture confirms the results of high-energy XRD.

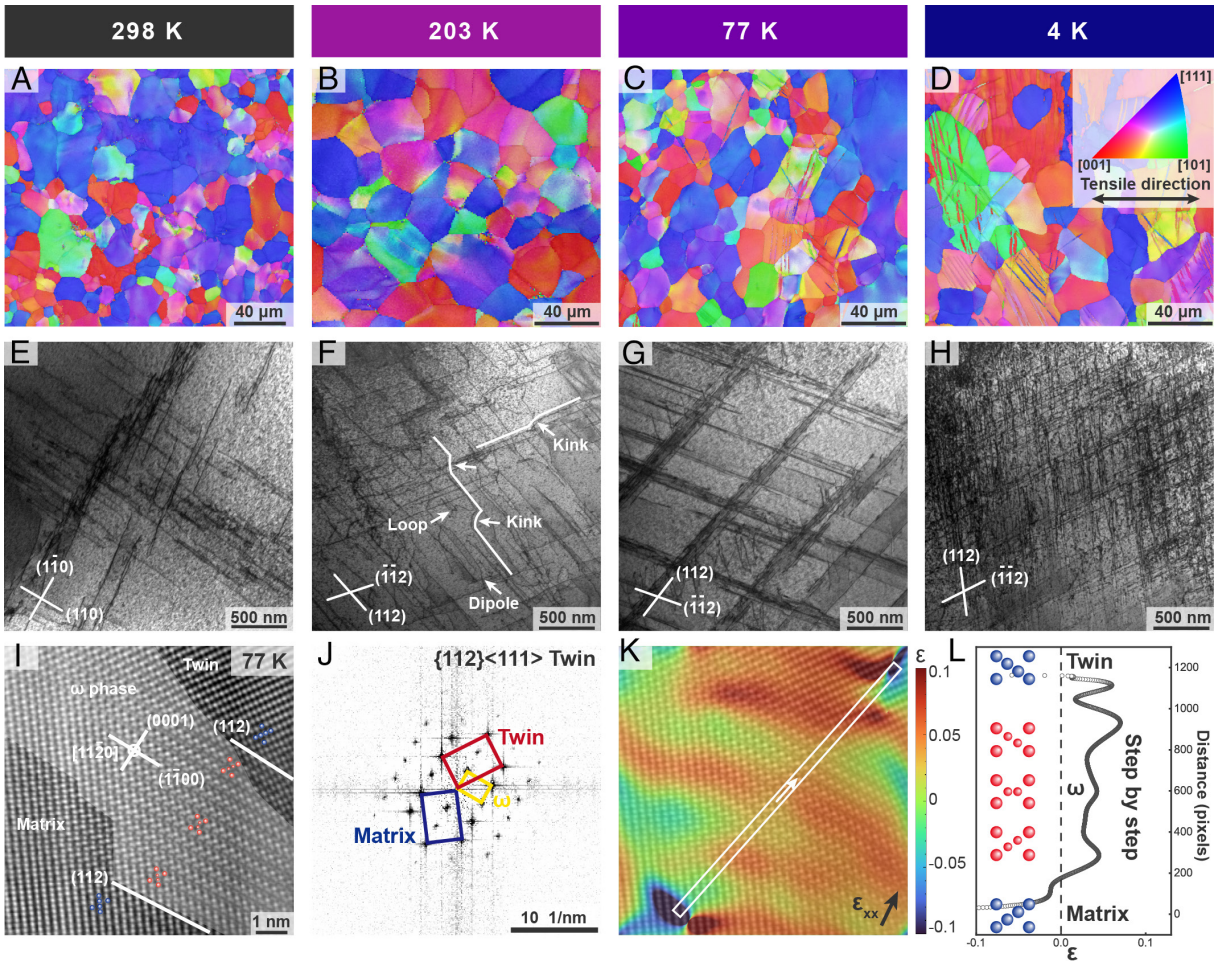

Fig. 3. The synergy mechanism between kinking of screw dislocations and deformation twinning for Nb40 during cryogenic deformation. (*A*) 298 K, (*B*) 203 K, (*C*) 77 K, and (*D*) 4 K EBSD inverse pole figure (IPF) after tensile fracture. During the 298 to 203 K temperature range, grain distortion dominates deformation, while {112}<111> deformation twins participate in the 77 to 4 K range. Dislocation morphology at (*E*) 298 K, (*F*) 203 K, (*G*) 77 K, and (*H*) 4 K and 1% strain, long straight 1/2[111] screw dislocations glide on {112} planes, overcome resistance via kink mode at cryogenic temperature. (*I*) High-resolution STEM of ω phase mediated twin nucleation through multistep shuffling at 77 K, 1% strain. (*J*) Corresponding fast Fourier transform (FFT) and (*K*) geometric phase analysis (GPA) map overlaid with atomic image; the strain of the white box is summarized in (*L*), which reveals the process of twin nucleation.

concentration while coordinating plastic strain. The interactions between kinked segments produce an additional source of strengthening, which manifests as the higher macroscopic flow stress observed in Fig. 1. As the temperature decreases further, intensified lattice friction would pin dislocation kinking. However, the difference in critical resolved shear stress between screw and nonscrew dislocations has been significantly reduced at ultralow temperatures due to the chemical fluctuation of high-entropy alloys (40). Multiple types of dislocations are activated, thereby achieving homogeneous deformation (41). Notably, the kink observed in Fig. 3*F* is about 100 nm in length, which is much larger than predicted from the classical Peierls mechanism. It is postulated that the rapid and jerky motion of screw dislocations at reduced temperature (42, 43) enhances the length-scale of kinks.

Between 77 K and 4 K, kink-dominated slip intensifies and localized slip-bundles appear. Meanwhile, {112}<111> deformation twins emerge (*SI Appendix*, Fig. S9), effectively alleviating stress concentration and enhancing plasticity. Twinning activity increases with decreasing temperature in the current study. Moreover, the omega phase typically appears at tips or boundaries with $\{112\}_{BCC}$//$\{1\text{–}100\}_{\omega}$, $<1\text{–}10>_{BCC}$//$<11\text{–}20>_{\omega}$, orientation relationships (*SI Appendix*, Figs. S10 and S11), promoting twin nucleation and reducing the critical resolved shear stress. This BCC-ω phase transformation reduces the energy barrier for twin nucleation via a step-by-step atomic shuffle mechanism, serving as a twinning pathway for high stacking-fault energy (SFE) BCC alloys (5), which is also evidenced by atomic-resolution scanning transmission electron microscopy (STEM) imaging (Fig. 3 *I–L*). In short, at cryogenic temperatures, the cooperative action of kink formation and twinning supplies an adaptive deformation channel that suppresses a brittle transition and preserves ductility.

The deformation mechanisms at elevated temperatures exhibit distinct characteristics (Fig. 4). At 1073 K, deformation primarily manifests through grain distortion (Fig. 4*A*). Noncontinuous dynamic recrystallization produces a necklace-like microstructure at 1273 K (Fig. 4*B*), where ultrafine grains slightly reduce the average grain size. When the temperature rises to 1473 K, complete dynamic recrystallization occurs through near-synchronous grain deformation (Fig. 4*C*), whereas dynamic recrystallization coexists with grain coarsening at 1673 K (Fig. 4*D*). Specifically, grain coarsening leads to enhanced superplastic deformation, contrary to the previously held belief that coarsening causes a drastic deterioration in plastic deformability (44). This intensive recrystallization-induced superplasticity phenomenon is concurrently manifested in the work hardening curve (*SI Appendix*, Fig. S13). Additionally, high-temperature oxidation-induced pores within the specimen become ultimate failure sources (*SI Appendix*, Fig. S3).

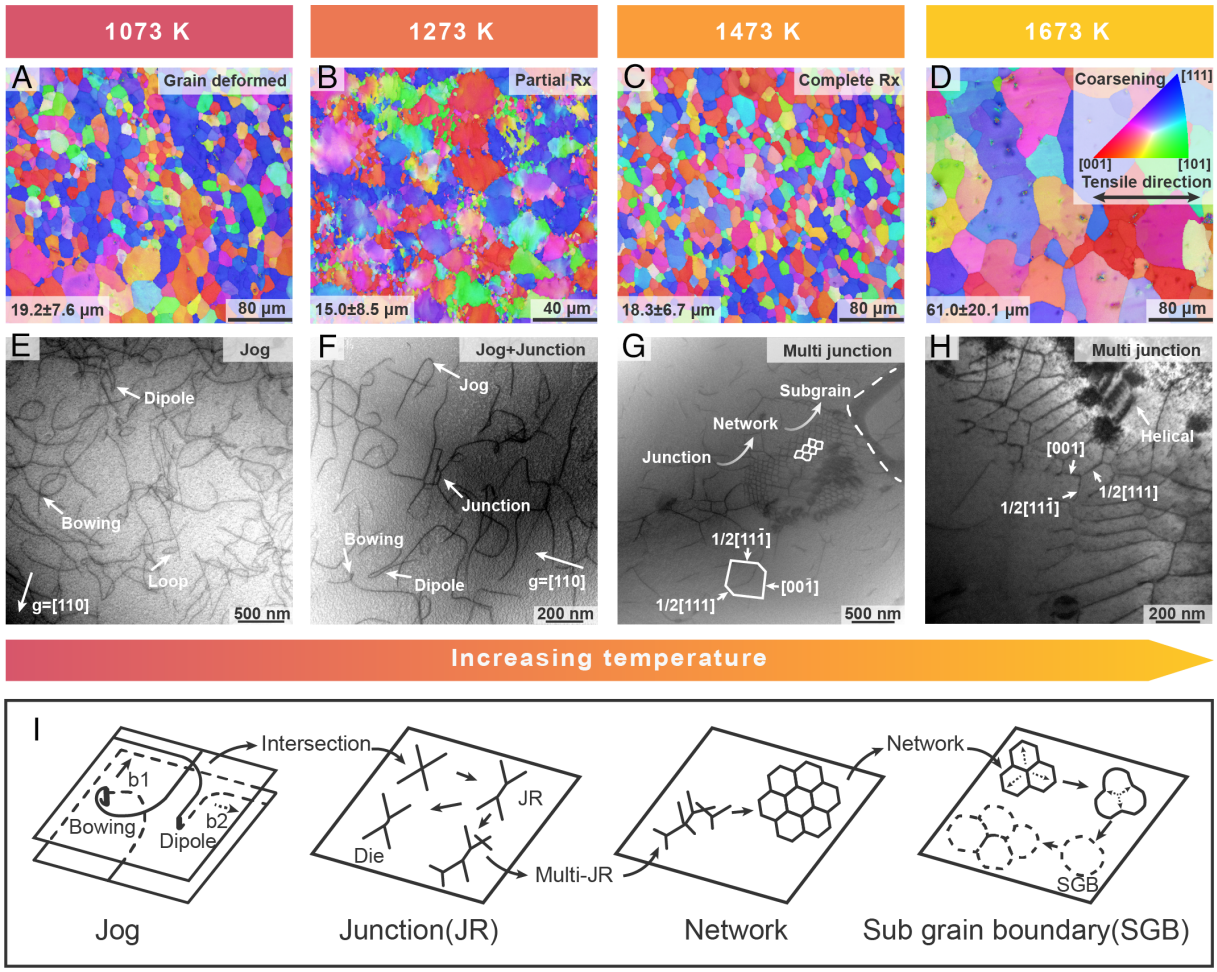

Fig. 4. The synergistic mechanism between dislocation jog and junction of Nb40 alloy during elevated-temperature deformation. EBSD IPF after tensile failure at (*A*) 1073 K, (*B*) 1273 K, (*C*) 1473 K, and (*D*) 1673 K, with corresponding average grain size marked in the bottom left corners. The deformation mechanism progressively transitions from grain distortion to partial recrystallization (partial Rx), complete recrystallization (complete Rx), and grain coarsening. The dislocation analysis of 1% strain at (*E*) 1073 K, (*F*) 1273 K, (*G*) 1473 K, and (*H*) 1673 K reveals shifts from jog to junction mechanisms with increasing temperature. (*I*) Schematic illustration of dislocation evolution mechanisms at high temperatures. As temperature increases, dislocations depart from original slip planes to form jogs, thereby generating an increased probability of dislocation intersection. These intersections would evolve into metastable dislocation junctions under a specific environment, which may either annihilate during subsequent deformation or interact with additional dislocations to form multijunctions and stabilized dislocation networks. The network provides favorable sites for subgrain boundary formation, driving the occurrence of dynamic recrystallization.

In sharp contrast to ambient-to-cryogenic temperatures, dislocation jogs are the primary features of dislocation morphology at elevated temperatures. These jogs have different effects on alloys due to their height, with possible configurations including vacancies, dislocation dipoles, and elongated super jogs (45) (Fig. 4*E* and *SI Appendix*, Fig. S14). The further evolution of dipoles produces prismatic dislocation loops (46), whose motion relies on vacancy aggregation to supply the climb force. In summary, the dominant jog mechanism at 1073 K induces strengthening through multiple pathways, enabling the alloy to exhibit a significant work-hardening effect, albeit sacrificing some plastic capability, which is also proven to be an effective strengthening strategy during long-term high-temperature creep (7) and in the cryogenic ductile-to-brittle transition (47). Specifically, this strengthening effect is only available within a relatively narrow temperature range (48), and ceases to be effective at approximately $0.6T_m$ (T_m is the melting point) as the increasing temperatures promote vacancy nucleation (49).

Microscopically, sustained motion and interaction of jogged segments produce stable junctions which commonly are composed of two ½[111] dislocations with one [100] component (Fig. 4*F*) (16). These junctions interconnect at higher temperatures to form multijunction structures and extended dislocation networks that act as precursors for subgrain boundary formation (50) and recrystallization (Fig. 4 *G* and *H* and *SI Appendix*, Figs. S15 and S16). Although simple theoretical treatments predict instability for some of these junctions in BCC metals, both experiments and atomistic simulations in Nb (15) and Mo (16) demonstrate that such metastable junctions can exist under dynamic conditions and can be highly mobile. Rapid junction migration accommodates plastic strain while promoting dislocation reactions that reduce the net dislocation density and seed subgrain boundaries (*SI Appendix*, Fig. S17), thereby facilitating continued flow and ultimately superplasticity. Schematic illustrations of dislocation jogs evolving into junctions, networks, and eventually subgrains are depicted in Fig. 4*I*.

Discussion

Dislocation Kinking and Omega Phase–Mediated Twinning Empower Cryogenic Properties. In BCC alloys, twin nucleation mechanisms are generally categorized into shear and shuffle pathways (51, 52). The shear mechanism typically involves the dislocation reaction of 1/6 <111> partial dislocations, which shear

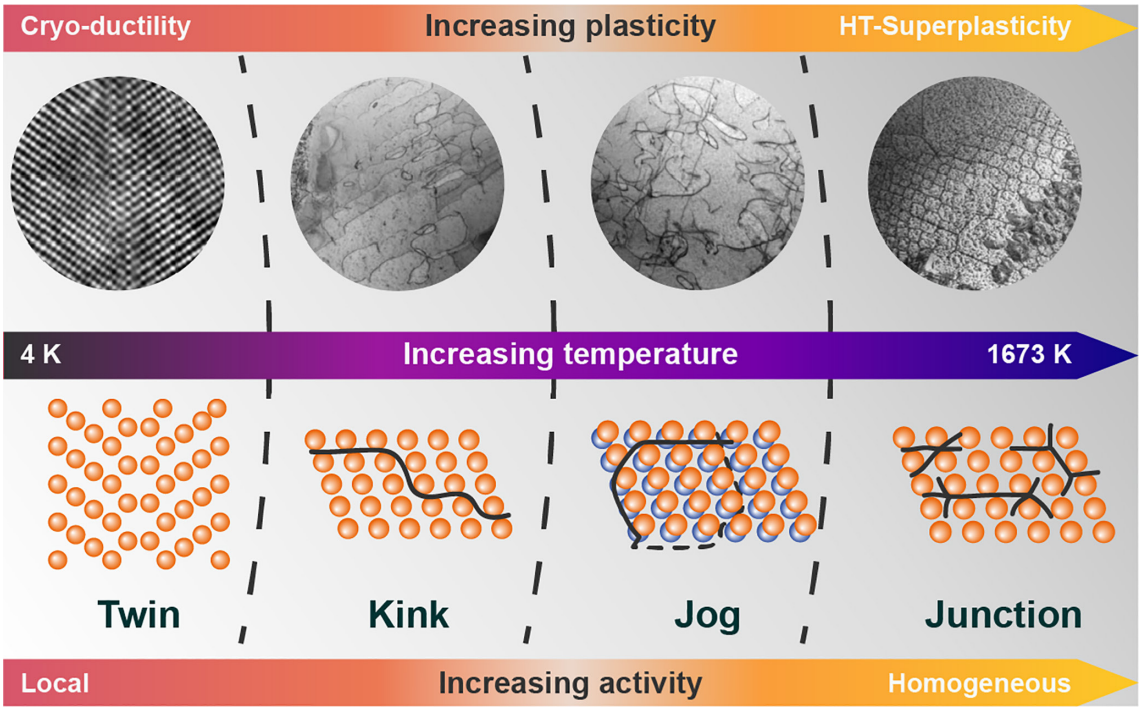

Fig. 5. The sequential activation of various deformation mechanisms for Nb40 alloy during the 1670 K temperature range. As temperature increases, twinning-induced plasticity (TWIP), dislocation kink, dislocation jog, and dislocation junction mechanisms are sequentially activated. Moreover, dislocation mechanisms exhibit higher mobility at higher temperature. Within a specific temperature range, several deformation mechanisms synergistically compete, collectively enabling an exceptional strength-ductility synergy throughout the ultrawide cryogenic-to-elevated temperature range.

through the matrix to create mirror-symmetric structures (53). For alloys with high stacking-fault energy that resist dislocation reaction, twin nucleation can alternatively proceed via an atomic shuffle mechanism. Notably, the ω phase transformation in BCC systems has been demonstrated through laser shock peening (54) and shear band (55) to occur via a shuffle mechanism. Investigations in pure Nb (56) and NbTaTiZr (57) systems further confirm the intrinsic correlation between this phase transformation and twin nucleation. Our high-resolution (HR) STEM observations and corresponding geometric phase analysis (GPA) (Fig. 3 *I–L*) demonstrate that the ω phase mediates twin nucleation through a multistep atomic shuffle, effectively reducing the resistance of BCC-twin transformation.

Under cryogenic conditions, the diminished mobility of screw dislocations confines their residence primarily to original slip planes, rendering a long and straight dislocation morphology. The motion of these dislocations necessitates kink-mediated slip. Compared to dilute metals, the multicomponent alloys provide more nucleation sites for dislocation kinks owing to the rugged energy landscape of the slip plane. As such, the motion of these complex kinks is impeded (40, 48), enhancing the strength of materials. At ultralow temperatures approaching absolute zero (4 K), the thermal vibration of atoms is drastically reduced, and thermally activated dislocation motion is significantly constrained (58). A multicomponent environment exhibits a dislocation pinning effect analogous to solute atmospheres. A further increase in strength causes a sudden depinning of this localized strengthening effect, releasing stress concentrations. This process generates microdeformation band structures and macroserrated curves (*SI Appendix*, Fig. S12) (59). The serration flow phenomenon, dominated by dislocation mechanisms, strengthens the alloy but reduces its plasticity. In addition, the accumulation of a local dislocation pile-up leads to planar slip, which accelerates plastic failure. Fortunately, deformation twinning can be activated, which partially suppresses such localized deformation through crystal reorientation, thereby enhancing the alloy's plastic capability (60). The competitive yet complementary relationship between dislocation kink and TWIP mechanisms fundamentally governs the low-temperature performance of this alloy.

Dislocation Reactions Induced High-Temperature Superplasticity. Dislocation mobility is largely enhanced at elevated temperatures, which manifests in two primary aspects. On the one hand, dislocations can deviate from their original slip planes, generating jogs that profoundly influence dislocation dynamic and macroscopic mechanical properties. On the other hand, the increased complexity of dislocation configurations leads to intensified interaction among defects. Distinct morphologies including dislocation dipoles, dislocation loops, and helical dislocations (*SI Appendix*, Fig. S19) coexist, collectively defining the fundamental characteristics of high-temperature dislocation architectures. These effects enable the occurrence of 1/2 <111> + 1/2 <1-1-1> = <100> dislocation reactions and the formation of metastable dislocation junctions which are composed of two different 1/2 <111> dislocations and one <100> dislocation. Deformation at elevated temperatures promotes massive and persistent generations that promote dislocation junctions, which progressively interconnect to establish stabilized dislocation networks composed of the same dislocation characters along specific crystallographic directions. The accumulation and evolution of such networks induce localized orientation fluctuations that serve as preferential nucleation sites for subgrain boundaries. The development of these dislocation configurations ultimately drives dynamic recrystallization of the microstructure while simultaneously enabling macroscopic superplasticity behavior in this alloy. This complex interplay of dislocations provides essential experimental data to calibrate and refine existing models for predicting high-temperature strength in refractory alloy systems (40).

It should be noted here that it is the belief of conventional metallurgy that in high stacking fault energy (SFE) metals, cross-slip of screw dislocations and climb of edge dislocations can occur

preferentially, with dynamic recovery dominating at elevated temperatures. In contrast, dynamic recrystallization predominantly governs deformation in low SFE systems. However, this work for the NbTaTi system has confirmed that dynamic recrystallization dominates high-temperature deformation in high SFE systems (5). At elevated temperatures, dislocation junctions and networks are rapidly activated, which provides the driving force for dynamic recrystallization. This recrystallization process, in turn, serves as the dominant mechanism for releasing stress concentration and sustaining superplastic deformation. Additionally, the unstable grain boundary structures may result in grain boundary sliding, which accelerates the superplasticity (6). Nevertheless, the unconventional dislocation morphing-derived high-temperature deformation is responsible for the enhanced plasticity.

Self-Adaptive Dislocation Mechanism Within the ~1,670 K Temperature Spectrum. It has been established that dislocation activities profoundly influence the mechanical properties of the designed RHEA across various temperatures. At cryogenic temperatures, a large Peierls barrier and reduced thermal activation render the domination of long straight dislocations whose motion requires kink or kink-pair formations, while the rugged chemical landscape in the Nb40 alloy provides massive nucleation sites for kinking (48). The interactions between kinks on distinctive slip planes give rise to dipoles and jogs (or cross-kinks) (Fig. 3*F*), effectively pinning dislocation motion. As the temperature rises, these interactions become more frequent due to enhanced thermal activation, leading to strengthening of the material and short curved dislocation morphologies at ambient to intermediate temperatures. However, increasing vacancy migration at elevated temperature rapidly renders this strengthening ineffective and promotes the formation of dislocation junctions, networks, and eventually subgrains and recrystallization. The complex composition of RHEA amplifies this mechanism by promoting vacancy migration and dislocation interactions. The self-adaption of dislocations in response to specific thermal conditions results in distinctive dislocation configurations (Fig. 5), which serve to ductilize the Nb40 model alloy across an ultrawide temperature spectrum.

Conclusions

This work unveils a model NbTaTi-based RHEA that defies conventional limits, delivering an exceptional strength-ductility synergy across a staggering 4 to 1,673 K temperature range via self-adaptive dislocation morphing. At cryogenic temperatures, kinked dislocation and omega-phase-aided {112}<111> twinning mechanisms act to overcome brittleness. At room temperature, sequential activation of edge-screw bolsters work hardening. At high temperatures, dislocation jogs and reactions evolve into junctions and networks, which contribute to superplasticity (up to 250% tensile elongation). Crucially, these mode switches are simply thermally activated and are stabilized by the multicomponent solid-solution chemistry, whose rugged chemical landscape renders otherwise transient defect assemblies robust. This continuous, self-adaptive dislocation mechanism, sequentially morphing from edge-screw (ambient) to kink-twin (cryogenic) to jog-junction (high-temperature), resolves the traditional cryogenic *vs*. high-temperature trade-off and provides a concrete mechanistic roadmap for advanced RHEAs. This work demonstrates the importance of integrating dislocation engineering with compositional design to empower precise control of defect mobility, interactions, and forms for targeted thermal regimes, advancing materials design for aerospace propulsion, fusion energy, and deep-space exploration.

Materials and Methods

Materials Preparation. The $Nb_{40}Ta_{25}Ti_{15}Hf_{15}Zr_5$ (Nb40 alloy) was prepared in a levitation furnace with 500 g of raw materials with 99.99% purity. The ingot was remelted 8 times to ensure elemental homogenization, resulting in a cylindrical cast, approximately 40 mm in diameter and 40 mm in height. The as-cast ingot was sectioned into 20 to 30 mm thick samples using a wire electrical discharge machine, followed by 80% reduction rolling (*SI Appendix*, Fig. S1). Subsequent annealing at 1,323 K for 1 h was performed to achieve equiaxed grain structure (*SI Appendix*, Fig. S2).

Mechanical Testing. Mechanical testing specimens were all dog-bone-shaped with equiaxed grains processed by wire electrical discharge machining. All tensile tests were conducted at a strain rate of 10^{-3} s^{-1}, with each temperature test conducted twice. The gauge dimension of tensile samples for room temperature (RT, 298 K), 203 K, and 77 K tests was 1.5 mm (width) × 1.5 mm (thickness) × 17 mm (length). Tests at 298 and 203 K employed an ETM504C Universal Testing Machine with strain measured using a 10 mm gauge length mechanical extensometer. The 203 K temperature environment was provided by an EMC003A-1 environmental chamber, while the 77 K condition was achieved using a foam-insulated liquid nitrogen container. For the 4 K test, the gauge dimension of a specimen was 3 mm (width) × 1.5 mm (thickness) × 16 mm (length), loaded on a SUNS UTM5305S tensile testing machine within a custom-built Dewar system; temperature was monitored by rhodium-iron thermometer. Strain was measured with a 10 mm gauge length mechanical extensometer. For high-temperature tests, the gauge dimensions of specimens were 3 mm (width) × 1.5 mm (thickness) × 33 mm (length); the tests were conducted on a UDL-50 high-temperature tensile testing machine, *in vacuo* (pressure ≤ 10^{-3} bar) to minimize oxidation, using Mo-Re alloy fixtures and a 25 mm gauge length mechanical extensometer. All specimens were maintained for 15 min at target temperatures prior to testing. Interrupted tests were manually terminated upon reaching the set strain, followed by immediate stress release and specimen recovery at room temperature.

Microstructural Characterization. X-ray diffraction (XRD) analysis was performed on a Bruker D8 Advance two-dimensional XRD system using Cu Kα radiation (50 kV, 1 mA) with a 20-degree step size. Specimens were sequentially ground with 400, 800, and 1,200 grit SiC papers. Electron backscatter diffraction (EBSD) specimens underwent progressive polishing. Specifically, samples were ground 400 to 4,000 grit SiC papers, mechanically polished with 3 μm, 1 μm, and 0.05 μm diamond suspensions, and polished for 8 to 10 h using a VP430 vibration polishing machine. Samples were finally argon ion polished with an IM4000II system at sequentially reduced voltages of 5 kV, 4 kV, and 3 kV, at an angle of 6 degrees for each step, with a duration of 1 h per step. EBSD characterization was conducted in an Apreso S Lovac Scanning Electron Microscope (SEM) equipped with an EDAX detector. The analysis software used for EBSD was ATEX (61).

Dislocation Characterization and Analysis. TEM specimens were prepared using an electrical discharge wire machine to obtain a 0.5 mm thickness and thinned to 50 μm through mechanical grinding (400 to 4,000 grit SiC papers). Standard specimens with 3 mm diameter were punched or glued onto 3 mm diameter Mo rings for smaller samples. Final thinning was achieved by a Gatan 691 precision ion polishing system, with a voltage of 5 kV and 8 degrees gun angle. Once the electron beam penetrated the sample and a small hole appeared, the voltage was reduced to 3.5 kV and 3 degrees gun angle for an additional 30 minutes of thinning to optimize the quality of the thin area. TEM characterization was conducted using FEI Tecnai G2 F20 and FEI Talos F200X microscopes, with spherical aberration-corrected imaging performed on a FEI Themis Z microscope. Dislocation analysis was performed according to the $g \cdot b$ criterion, where g is the operating diffraction vector and b is the Burgers vector of the dislocation. GPA of high-resolution images was implemented using the pair–pair algorithm (62) in the Strain++ software.

Synchrotron High-Energy XRD. High-energy X-ray diffraction experiments were conducted on the ultrahard X-ray multifunctional application beamline at the Shanghai Synchrotron Radiation Facility (SSRF). The X-ray wavelength employed was

0.1258 Å, with a scattering angle between 0.1087 and 7 degrees, and beam size of 500 × 500 μm^2. We utilized standard CeO_2 to correct the instrumental effect. In situ tension samples were designed with a gauge section 3 mm in width, 1.5 mm thick, and 33 mm in length. Tensile tests were performed at a strain rate of $1.5 \times 10^{-4}\ s^{-1}$. Data collection utilized a PILATUS3 X CdTe 2 M detector with an exposure time of 10 s. A schematic of the experimental set-up is shown in Fig. 2*A*. Two-dimensional Debye rings were processed using the Fit2D software to extract the intensity-2θ profile (*SI Appendix*, Fig. S4)(63). Peak broadening parameters were obtained by the fitting of a Gaussian function.

Using the modified Williamson-Hall method (19), dislocation activities at different strains were analyzed. Diffraction peak broadening primarily arises from two contributions: effects of crystallization size and of dislocation-induced microstrain. The simplified equation can be expressed as

$$(\Delta K)^2 = \left(\frac{0.9}{D}\right)^2 + \left(\frac{\pi A^2 b^2 \rho}{2}\right) K^2 C_{hkl} + O\left(K^2 C_{hkl}\right)^2,$$

where ΔK and K are broadening-related parameters, $K = \frac{2\ sin\ \theta}{\lambda}, \Delta K = \frac{2\ cos\ \theta(\Delta\theta)}{\lambda}$, θ, $\Delta\theta$, and λ are the Bragg angle, full-width-at-half-maximum (FWHM), and X-ray wavelength, respectively. D is the crystallite size, and A, b, and ρ are the outer cutoff radius of dislocations, magnitude of the Burgers vector and dislocation density, respectively. C_{hkl} is the dislocation contrast factor, which is dependent on dislocation type. O is higher-order term of $K^2 C_{hkl}$ and is generally negligible.

$$C_{hkl} = C_{h00}\left[1 - q\left(\frac{h^2k^2 + k^2l^2 + h^2l^2}{\left(h^2 + k^2 + l^2\right)^2}\right)\right].$$

Both C_{h00} and q are constants dependent on dislocation type, where h, k, and l denote the diffraction planes. The calculation of dislocation contrast factors requires the elastic constants of the Nb40 alloy; these were determined as C_{11} = 212.62 GPa, C_{12} = 129.42 GPa, C_{44} = 48.28 GPa by mixing the pure elements (20). Using the ANIZC software (64), calculations indicated that C_{h00} = 0.185 and $q = -0.129$ for <111>{110} for edge dislocations, and C_{h00} = 0.236 and q = 2.162 for <111>screw dislocations, thereby obtaining the contrast factor for the pure dislocation type (38). Linear fitting of $(\Delta K)^2$ versus $K^2 C_{hkl}$ was performed, such that the evolution of dislocation activity could be determined by statistically analyzing the R^2 values for pure dislocations by fitting at different strains.

Data, Materials, and Software Availability. All study data are included in the article and/or *SI Appendix*.

ACKNOWLEDGMENTS. We acknowledge the financial support of this research by the National Natural Science Foundation of China under Grant No. 52571119, Zhejiang Provincial Natural Science Foundation of China under Grant No. LD24E010005, and Shanghai Key Laboratory of Material Frontiers Research in Extreme Environments, China (No. 22dz2260800). We also thank the BL12SW station and the User Experiment Assist System of the Shanghai Synchrotron Radiation Facility (SSRF) for help in characterization and Prof. Shan-Dong Tu of the East China University of Science and Technology for his additional review of the manuscript.

Author affiliations: [a]Key Laboratory of High-temperature Structural Materials and Coating Technology (Ministry of Industry and Information Technology), School of Materials Science and Engineering, Beihang University, Beijing 102206, China; [b]Tianmushan Laboratory, Beihang University, Hangzhou 311115, China; [c]Center for High Pressure Science and Technology Advanced Research, Shanghai 201203, China; [d]Shanghai Key Laboratory of Material Frontiers Research in Extreme Environments, Institute for Shanghai Advanced Research in Physical Sciences, Shanghai 201203, China; and [e]Department of Materials Science and Engineering, University of California, Berkeley, CA 94720

1. J. H. Perepezko, The hotter the engine, the better. *Science* **326**, 1068–1069 (2009).
2. O. N. Senkov, G. B. Wilks, D. B. Miracle, C. P. Chuang, P. K. Liaw, Refractory high-entropy alloys. *Intermetallics* **18**, 1758–1765 (2010).
3. O. N. Senkov, J. M. Scott, S. V. Senkova, D. B. Miracle, C. F. Woodward, Microstructure and room temperature properties of a high-entropy TaNbHfZrTi alloy. *J. Alloys Compd.* **509**, 6043–6048 (2011).
4. C. Zhang *et al.*, Strong and ductile refractory high-entropy alloys with super formability. *Acta Materialia* **245**, 118602 (2022), 10.1016/j.actamat.2022.118602.
5. D. H. Cook *et al.*, Kink bands promote exceptional fracture resistance in a NbTaTiHf refractory medium-entropy alloy. *Science* **384**, 178–184 (2024).
6. C.-J. Liu *et al.*, Tensile creep behavior of HfNbTaTiZr refractory high entropy alloy at elevated temperatures. *Acta Mater.* **237**, 118188 (2022).
7. G. Sahragard-Monfared *et al.*, Tensile creep behavior of the Nb45Ta25Ti15Hf15 refractory high entropy alloy. *Acta Mater.* **272**, 119940 (2024).
8. Y. Yan, K. A. McGarrity, D. J. Delia, C. Fekety, K. Wang, The oxidation-resistance mechanism of WTaNbTiAl refractory high entropy alloy. *Corros. Sci.* **204**, 110377 (2022).
9. X. Wang, W. Bai, Z. Zhang, Z. Wang, X. Ren, Enhancing fatigue resistance of high-entropy alloy by designing a hierarchically heterogeneous microstructure. *J. Mater. Res. Technol.* **33**, 673–682 (2024).
10. M. A. Khan *et al.*, Influence of high-strain-rate compression and subsequent heat treatment on (TiNbZr)89(AlTa)11 refractory high-entropy alloys: Dynamic-mechanical behavior and microstructural changes. *Mater. Des.* **243**, 113062 (2024).
11. S. Dangwal, K. Edalati, Developing a single-phase and nanograined refractory high-entropy alloy ZrHfNbTaW with ultrahigh hardness by phase transformation via high-pressure torsion. *J. Alloys Compd.* **1010**, 178274 (2025).
12. P. M. Anderson, J. P. Hirth, J. Lothe, *Theory of Dislocations* (Cambridge University Press, 2017).
13. Y. Aono, E. Kuramoto, K. Kitajima, Orientation dependence of slip in niobium single crystals at 4.2 and 77 K. *Scr. Metall.* **18**, 201–205 (1984).
14. M. I. Wood, G. Taylor, Niobium–an athermal plateau in the low-temperature yield stress. *Philos. Mag. A* **56**, 329–342 (1987).
15. D. Caillard, B. Bienvenu, E. Clouet, Anomalous slip in body-centred cubic metals. *Nature* **609**, 936–941 (2022).
16. V. V. Bulatov *et al.*, Dislocation multi-junctions and strain hardening. *Nature* **440**, 1174–1178 (2006).
17. F. Wang *et al.*, Multiplicity of dislocation pathways in a refractory multiprincipal element alloy. *Science* **370**, 95–101 (2020).
18. T. Tsuru *et al.*, Intrinsic factors responsible for brittle versus ductile nature of refractory high-entropy alloys. *Nat. Commun.* **15**, 1706 (2024).
19. C. Lee *et al.*, Temperature dependence of elastic and plastic deformation behavior of a refractory high-entropy alloy. *Sci. Adv.* **6**, eaaz4748 (2020).
20. C. Lee *et al.*, Strength can be controlled by edge dislocations in refractory high-entropy alloys. *Nat. Commun.* **12**, 5474 (2021).
21. R. Feng *et al.*, Superior high-temperature strength in a supersaturated refractory high-entropy alloy. *Adv. Mater.* **33**, 2102401 (2021).
22. Z. Lei *et al.*, Enhanced strength and ductility in a high-entropy alloy via ordered oxygen complexes. *Nature* **563**, 546–550 (2018).
23. Z. An *et al.*, Negative mixing enthalpy solid solutions deliver high strength and ductility. *Nature* **625**, 697–702 (2024), 10.1038/s41586-023-06894-9.
24. L. Wang *et al.*, Tailoring planar slip to achieve pure metal-like ductility in body-centred-cubic multi-principal element alloys. *Nat. Mater.* **22**, 950–957 (2023), 10.1038/s41563-023-01517-0.
25. S. Wang *et al.*, TiZrHfNb refractory high-entropy alloys with twinning-induced plasticity. *J. Mater. Sci. Technol.* **187**, 72–85 (2024).
26. A. Sengupta *et al.*, Tensile behavior of a new single-crystal nickel-based superalloy (CMSX-4) at room and elevated temperatures. *JMEP* **3**, 73–81 (1994).
27. O. N. Senkov, S. I. Rao, D. B. Miracle, A. E. Mann, A. Yousefiani, Effect of Re and Al additions on the microstructure and mechanical properties of Nb-18Ti-12W alloy. *Mater. Sci. Eng. A.* **870**, 144870 (2023).
28. C. T. Liu, H. Inouye, Mechanical properties and interstitial contamination in a molybdenum-base alloy *Int. J. Refract. Metals Hard Mater.* **109**, 105971 (1973).
29. O. N. Senkov, J. Gild, T. M. Butler, Microstructure, mechanical properties and oxidation behavior of NbTaTi and NbTaZr refractory alloys. *J. Alloys Compd.* **862**, 158003 (2021).
30. C. Lee *et al.*, Deformation behaviors in single BCC-phase refractory multi-principal element alloys under dynamic conditions. *Adv. Sci.* **12**, e08180 (2025).
31. B. Xiao *et al.*, Superior strength-ductility synergy in TiZrNbVAl high entropy alloys via additive manufacturing. *Acta Mater.* **298**, 121389 (2025).
32. O. N. Senkov *et al.*, Microstructure and elevated temperature properties of a refractory TaNbHfZrTi alloy. *J. Mater. Sci.* **47**, 4062–4074 (2012).
33. T. G. Nieh, J. Wadsworth, O. D. Sherby, *Superplasticity in Metals and Ceramics* (Cambridge University Press UK, 1997).
34. X. Yan, Y. Zhang, Y. Zou, Near-superplastic behavior of a body-centered cubic Zr50Ti35Nb15 multi-principal element alloy via dynamic recrystallization. *Scripta Mater.* **227**, 115308 (2023).
35. Q. Wang, J. Wang, J. Li, Z. Zhang, S. X. Mao, Consecutive crystallographic reorientations and superplasticity in body-centered cubic niobium nanowires. *Sci. Adv.* **4**, eaas8850 (2018).
36. W. Chen *et al.*, Revealing the room temperature superplasticity in bulk recrystallized molybdenum. *Nat. Commun.* **14**, 8336 (2023).
37. T. Ungár, A. Borbély, The effect of dislocation contrast on x-ray line broadening: A new approach to line profile analysis. *Appl. Phys. Lett.* **69**, 3173–3175 (1996).
38. T. Ungár, I. Dragomir, Á. Révész, A. Borbély, The contrast factors of dislocations in cubic crystals: The dislocation model of strain anisotropy in practice. *J. Appl. Cryst.* **32**, 992–1002 (1999).
39. Y. W. Wang *et al.*, Ductilization of single-phase refractory high-entropy alloys via activation of edge dislocation. *Acta Mater.* **284**, 120614 (2025).
40. S. I. Rao *et al.*, Modeling solution hardening in BCC refractory complex concentrated alloys: Nbtizr, Nb1.5tizr0.5 and Nb0.5tizr1.5. *Acta Mater.* **168**, 222–236 (2019).
41. L. Lilensten *et al.*, Study of a bcc multi-principal element alloy: Tensile and simple shear properties and underlying deformation mechanisms. *Acta Mater.* **142**, 131–141 (2018).
42. D. Caillard, Kinetics of dislocations in pure Fe. Part II. In situ straining experiments at low temperature. *Acta Mater.* **58**, 3504–3515 (2010).
43. L. Proville, A. Choudhury, Unravelling the jerky glide of dislocations in body-centred cubic crystals. *Nat. Mater.* **23**, 47–51 (2024).

44. G. Liu *et al.*, Nanostructured high-strength molybdenum alloys with unprecedented tensile ductility. *Nat. Mater.* **12**, 344–350 (2013).
45. J. J. Gilman, W. G. Johnston, "Dislocations in Lithium Fluoride Crystals" in *Solid State Physics*, F. Seitz, D. Turnbull, Eds. (Academic Press, 1962), pp. 147–222.
46. A. S. Tetelman, Dislocation dipole formation in deformed crystals. *Acta Metall.* **10**, 813–820 (1962).
47. Y.-H. Zhang, E. Ma, J. Sun, W.-Z. Han, Unveiling the intrinsic rhenium effect in tungsten. *Acta Mater.* **264**, 119586 (2024).
48. F. Maresca, W. A. Curtin, Theory of screw dislocation strengthening in random BCC alloys from dilute to "High-Entropy" alloys. *Acta Mater.* **182**, 144–162 (2020).
49. O. N. Senkov, S. Gorsse, D. B. Miracle, High temperature strength of refractory complex concentrated alloys. *Acta Mater.* **175**, 394–405 (2019).
50. M. Kuzmina, M. Herbig, D. Ponge, S. Sandlöbes, D. Raabe, Linear complexions: Confined chemical and structural states at dislocations. *Science* **349**, 1080–1083 (2015).
51. J. W. Christian, S. Mahajan, Deformation twinning. *Prog. Mater. Sci.* **39**, 1–157 (1995).
52. X. Li, Z. Zhang, J. Wang, Deformation twinning in body-centered cubic metals and alloys. *Prog. Mater. Sci.* **139**, 101160 (2023).
53. B. A. Bilby, A. G. Crocker, The theory of the crystallography of deformation twinning. *Proc. R. Soc. Lond. A* **288**, 240–255 (1965).
54. L. Zhang *et al.*, Deformation-induced ω phase transition in polycrystalline tungsten under extreme shock loading. *Scripta Mater.* **256**, 116432 (2025).
55. X. Li *et al.*, Shear band mediated ω phase transformation in Nb single crystals deformed at 77 K. *Mater. Res. Lett.* **9**, 523–530 (2021).
56. X. Li *et al.*, Phase transformation induced transitional twin boundary in body-centered cubic metals. *Acta Mater.* **249**, 118815 (2023).
57. X. Zhang *et al.*, Deformation twinning in Ti48.9Zr32.0Nb12.6Ta6.5 medium entropy alloy. *Mater. Sci. Eng. A.* **809**, 140931 (2021).
58. A. S. Tirunilai *et al.*, Dislocation-based serrated plastic flow of high entropy alloys at cryogenic temperatures. *Acta Mater.* **200**, 980–991 (2020).
59. T. J. Jang *et al.*, Ultra-low temperature mechanical response of VCoNi medium-entropy alloy with unprecedented high strength and ductility. *Int. J. Plast.* **194**, 104473 (2025).
60. L. Zhong, Y. Zhang, X. Wang, T. Zhu, S. X. Mao, Atomic-scale observation of nucleation- and growth-controlled deformation twinning in body-centered cubic nanocrystals. *Nat. Commun.* **15**, 560 (2024).
61. B. Beausir, J.-J. Fundenberger, Analysis tools for electron and X-ray diffraction, ATEX–software. Deposited 2017 (2017).
62. M. J. Hÿtch, E. Snoeck, R. Kilaas, Quantitative measurement of displacement and strain fields from HREM micrographs. *Ultramicroscopy* **74**, 131–146 (1998).
63. A. P. Hammersley, FIT2Dâ€¯: A multi-purpose data reduction, analysis and visualization program. *J. Appl. Crystallogr.* **49**, 646–652 (2016).
64. A. Borbély, J. Dragomir-Cernatescu, G. Ribárik, T. Ungár, Computer program ANIZC for the calculation of diffraction contrast factors of dislocations in elastically anisotropic cubic, hexagonal and trigonal crystals. *J. Appl. Crystallogr.* **36**, 160–162 (2003).